Irradiation effects in high entropy alloys and 316H stainless steel at 300 °C

Wei-Ying Chen [a, *], Xiang Liu [b], Yiren Chen [a], Jien-Wei Yeh [c], Ko-Kai Tseng [c], Krishnamurti Natesan [a]

[a] Argonne National Laboratory, Lemnot, IL, USA
[b] University of Illinois, Urbana-Champaign, IL, USA
[c] National Tsing Hua University, Hsing-Chu, Taiwan

ARTICLE INFO

ABSTRACT

High entropy alloys (HEAs) have been considered for applications in nuclear reactors due to their promising mechanical properties, corrosion and radiation resistance. It has been suggested that sluggish diffusion kinetics and lattice distortion of HEAs can enhance the annihilation of irradiation-induced defects, giving rise to a higher degree of tolerance to irradiation damage. In order to understand the irradiation effects in HEAs and to demonstrate their potential advantages over conventional austenitic stainless steels (SS), we performed *in-situ* ion irradiation experiments with 1 MeV krypton at 300 °C on two HEAs and a 316H SS under an identical irradiation condition. The irradiation introduced a high density of dislocation loops in all materials, and the microstructural evolution as a function of dose was similar for HEAs and 316H SS. Nanoindentation tests showed that the degree of irradiation hardening was also comparable between them. The similar microstructural evolution and irradiation hardening behavior between the HEAs and 316H indicate that, at low temperatures (≤300 °C), the irradiation damage of fcc alloys is not sensitive to compositional variation and configurational entropy.

Published by Elsevier B.V.

1. Introduction

High entropy alloys (HEAs) have received great attention in research community because of their novel concept of alloy design, excellent strength and resistance to corrosion, wear, and softening at high temperatures [1,2]. As compared with conventional alloys that contain one principle element or compound, HEAs consist of five or more principle elements in nearly equimolar ratios, leading to a higher configurational entropy that enhances the phase stability and reduces the tendency of forming detrimental intermetallic phases at high temperatures. In addition, the diffusion kinetics in HEAs is suggested to be sluggish due to a large fluctuation in lattice sites potential [3], which is beneficial for stabilizing supersaturated states, improving creep resistance, slowing down grain growth, reducing particle coarsening rate, etc [4]. Severe lattice distortion is another characteristic of HEAs where significant stress and strain are resulted from the varied sizes of constituent

atoms. The lattice distortion can hinder dislocation motion, leading to a noticeable strengthening effect [5].

Recently, HEAs also attract attention in the field of nuclear materials due to their potential resistance to radiation damage [6–10]. The sluggish diffusion kinetics and distorted lattice could immobilize irradiation-induced point defects and hinder defect clustering. Immobilization of point defects is one of the proposed approaches to design radiation-resistant materials as suggested by Zinkle and Snead [11]. Experimentally, HEAs have been shown to exhibit less radiation-induced segregation (RIS) than conventional Fe-Cr-Ni alloys [9]. In addition, the radiation damage and swelling have been shown to decrease with increasing compositional complexity [6,12].

Although recent results about the irradiation performance of HEAs are promising, some crucial aspects are still lacking. Firstly, irradiation data comparing HEAs with commercial alloys are needed. Except for a study by Kumar et al. [9], most recent work compared HEAs with simpler equimolar alloys (i.e. binary, ternary etc.) [6,7,10,12]. As a new class of materials for nuclear applications, it is important to demonstrate that HEAs are competitive and can outperform current commercial alloys. Secondly, the evolution of

irradiation-induced dislocation loops in HEAs has not been studied extensively. Irradiation-induced dislocation loops are an important factor for irradiation hardening and embrittlement. In HEAs, whether or not a higher configurational entropy, more sluggish diffusion kinetics, and highly distorted lattice can naturally lead to a smaller mean size and lower density of dislocation loops, and therefore reduce the extent of irradiation hardening and embrittlement remains to be verified.

In addition, the results about the dependency of irradiation-induced dislocation loops with alloy composition are inconsistent among recent studies. For instance, Lu et al. reported a general trend of increasing loop density and decreasing loop size with increasing compositional complexity under 1.5–3 MeV nickel ion irradiations at 500 °C to ~4–60 dpa [6,7]. In contrast, Shi et al. observed an significantly different trend for the same materials irradiated at the same temperatures with 1 MeV krypton ions to 2 dpa [13]. When comparing HEAs (multi-principle-element alloys) with 316 SS (single-principle-element alloy), Kumar et al. [9] showed that the dislocation loops were smaller while density higher in irradiated HEAs than in 316 SS. These conflicting results on the impact of compositional complexity require further research.

This study aimed to investigate the evolution of irradiation-induced dislocation loops in HEAs at 300 °C. The irradiated microstructures of HEAs were compared with that of conventional 316 stainless steel to assess their irradiation response at low temperatures.

2. Experiment and data analysis

Two HEAs, CoCrFeMnNi and $Al_{0.3}$CoCrFeNi, and a conventional Type 316H SS (denoted as 316H thereafter) were investigated. All of them have a single-phase face-centered cubic (fcc) crystal structure. The CoCrFeMnNi and $Al_{0.3}$CoCrFeNi were selected because of their single-phase microstructure after homogenization [14,15]. These HEAs have been extensively studied for their mechanical, microstructural and thermodynamics properties [5,16]. The 316H was selected in this study as a reference conventional austenitic material. It is a high carbon version of 316 stainless steel, and has been used as the structural material in liquid-metal-cooled nuclear reactors [17]. Table 1 shows the nominal and the measured compositions of these materials.

The CoCrFeMnNi and $Al_{0.3}$CoCrFeNi were fabricated by arc melting at National Tsing Hua University. Details of the fabrication procedure can be found in Ref. [18]. The weight loss during arc-melting is insignificant as no constituent elements were volatile [19,20]. The solidified ingots of HEAs were cold-rolled by 70%, and subsequently homogenized at 1200 °C for 48 h, followed by water quench. The loss of aluminum during homogenization was negligible due to the dense and thermally-stable alumina protection, and the low vapor pressure at this temperature. As shown in Table 1, the composition of homogenized HEAs, as measured by

energy-dispersive x-ray spectroscopy (EDS), was close to the design value. The 316H was solution annealed at 1065 °C for 1 h and then water quenched.

Three-mm disks for transmission electron microscopy (TEM) were sectioned and punched from the as-received materials. The TEM disks were then mechanically thinned and electro-polished with an electrolyte of 50 mL perchloric acid and 950 mL methanol at −40 °C. The TEM thin foils were subsequently irradiated with 1 MeV krypton ions with a 15° incident angle at 300 °C to 1 dpa with a flux of 6.3×10^{15} ions/(m^2·s) under simultaneous TEM observation at the Intermediate-Voltage Electron Microscopy (IVEM)-Tandem facility of Argonne National Laboratory (ANL). The ion beam is homogeneous over an area of 1.5 mm in diameter. The microscope is a Hitachi-9000 TEM operated at 300 keV. As calculated with the Stopping and Range of Ions in Matter (SRIM) code [21] (Fig. 1), the damage and implantation profile of 1 MeV Kr ions are similar in the HEAs and 316H.

Irradiation-induced defects were recorded consistently with imaging conditions of weak-beam dark field (WBDF) (g = 200, 5−6 g) and bright field at 011 zone axis for all three materials. The size and density of dislocation loops were measured on WBDF micrographs of the same magnification with a scheme adapted from the procedures described by Yi et al. [22]. Firstly, the images were processed to remove background contrast due to thickness fringes. This was achieved by filtering an image through replacing each pixel (0.2 nm × 0.2 nm) with the median value of the neighboring pixels within 9.6 nm, and then subtracted the original image. In order to remove wild pixels that had artificially high intensity, the images were further smoothed with Gaussian blurring with a sigma radius of one pixel. The processed images were
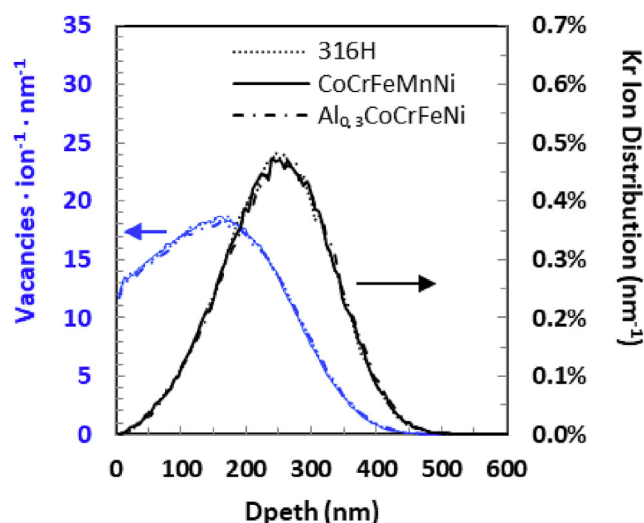

Fig. 1. SRIM calculation of the displacement damage and distributions of 1 MeV krypton ions in 316H, CoCrFeMnNi and $Al_{0.3}$CoCrFeNi.

Table 1
Nominal (measured) material compositions (at%).

	Fe	Cr	Ni	Mn	Co	Al	Mo	Si	C	N
$Al_{0.3}$CoCrFeNi										
Nominal (Measured)	23.3 (23.7)	23.3 (23.0)	23.3 (22.7)		23.3 (24.2)	6.8 (6.4)				
CoCrFeMnNi										
Nominal (Measured)	20 (20.4)	20 (19.8)	20 (19.8)	20 (19.3)	20 (20.8)					
316H[a]										
Nominal (Measured)	bal.	18.4 (18.3)	12.5 (12.5)	2.1 (2.0)			1.4 (1.4)	1.2 (1.0)	0.3 (n.m.)	0.1 (n.m.)

n.m.: Not measured.
[a] 316H also contains 0.04% V, 0.03% P, 0.03% S and <0.01% B nominally.

segmented into smaller ones and analyzed individually in order to further avoid the adverse effects of background.

The counting of loops was done by finding the local maximum with a designated noise tolerance using ImageJ. The noise tolerance was determined manually by winding down the parameter until the software picked up all dislocation loops. Similar to Ref. [22], we found that a variation of ±10 in grey scale reasonably represented the background fluctuation, and thus was adopted to account for the uncertainty of each measurement. The density of the loops was calculated by dividing the count with the foil thickness estimated from thickness contours. The maximum extent of loop image was measured as the size of the loop. Irradiation-induced voids were examined with through-focus technique.

Nanoindentation was performed on the as-received and ion-irradiated specimens at University of Illinois at Urbana-Champaign. The specimen preparation was the same as that for TEM specimens except for the final electro-polishing step. A fixed polishing time of 20 seconds was used to remove the thin deformed layer at surface resulted from mechanical polishing. Prior to the nanoindentation, the specimens were mounted on magnetic disks using super glue and dried for at least 5 hours. The nanoindentation was carried out on a Hysitron TI 950 Triboindenter with a Berkovich tip under quasi-static mode, using displacement control to a nominal maximum displacement of 100 nm. This displacement value was optimal to avoid an excessive size effect of shallow indentation and interference of soft substrate beyond irradiated zone. The size effect and the influence of soft substrate will be discussed more in section 3.3. The Indent spacing was 30 μm. At
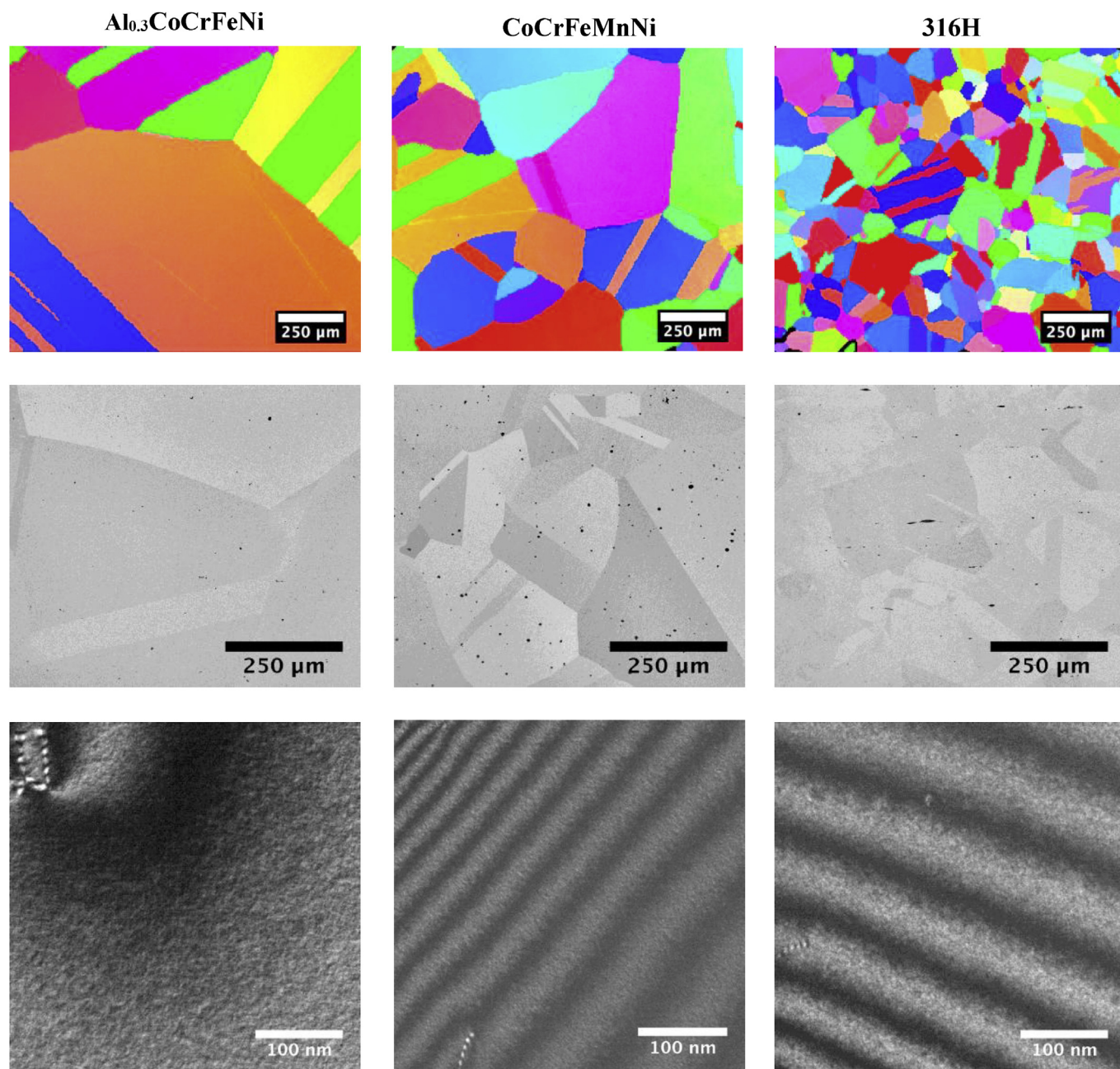

Fig. 2. The EBSD maps (1st row), backscattering electron SEM images (2nd row), and weak-beam dark field TEM images (3rd row) of the as-received $Al_{0.3}CoCrFeNi$, CoCrFeMnNi and 316H. The black particles in the backscattering electron SEM images are inclusions.

Table 2
Microstructural parameters of as-received specimens.

	$Al_{0.3}CoCrFeNi$	CoCrMnFeNi	316H
Grain size (μm)	~500	~400	~100
Inclusion volume fraction (%)	0.08	0.45	0.18
Dislocation Density (10^{12} m^{-2})	1.4	2.6	3.5

least 10 indents were performed for each specimen.

The grain size of 316H was measured by electron backscattering diffraction (EBSD) with an Oxford Instruments NordlysNano detector equipped on a Hitachi S-2700 SEM. The grain sizes of CoCrFeMnNi and $Al_{0.3}CoCrFeNi$ were larger than 316H, and were estimated with backscattering electron (BSE) images from a Hitachi S-4700 SEM in Center for Nanoscale Materials at ANL.

3. Results and discussion

3.1. Pre-irradiation characterization

As shown in the EBSD orientation maps in Fig. 2 and the grain size in Table 2, all three materials exhibited relatively large grain sizes with a few twins. The grain size of 316H was the smallest. Between the two HEAs, while having the same heat treatment, the grain size of CoCrFeMnNi was evidently smaller. This may be due to a number of factors such as the melting temperature (T/T_M), diffusion coefficient, uniformity of cold work and amount of

Fig. 3. EDS spectrum of the inclusions in (a) $Al_{0.3}CoCrFeNi$, (b) CoCrFeMnNi and (c) 316H.

inclusions.

As shown in the BSE images in Fig. 2, all materials contained thinly dispersed inclusions with lower Z-contrast. The corresponding volume fractions of the inclusions were given in Table 2. The inclusions were characterized with EDS as shown in Fig. 3. For $Al_{0.3}CoCrFeNi$, the inclusions were aluminum oxides. The amount was negligibly low. For CoCrFeMnNi, the inclusions were Cr-rich and Mn-rich oxides. The oxide content in the raw manganese material of CoCrFeMnNi gave rise to its higher amount of oxide inclusions (as compared with $Al_{0.3}CoCrFeNi$). For 316H, the elongated inclusions were MnS precipitates, which are common in stainless steels. Because of their very low density, the inclusions in HEAs and 316H were generally not observed in the electron-transparent regions of the thin foil during in-situ TEM experiments, and their effects on the irradiation process were insignificant.

Disregarding the minor inclusions, the as-received materials were single-phase fcc with no observable ordered phases (e.g. L1$_2$ [23]) or other secondary phases as shown in the TEM micrographs in Fig. 2 and the diffraction patterns in Fig. 4. The dislocation densities in HEAs and 316H were measured with the equation

$$\rho = \frac{4}{\pi} \frac{\ell}{At}$$

where ρ is dislocation density, ℓ is the projected length of dislocations, A is the measured area and t is the foil thickness. As shown in Table 2, the dislocation density was in the order of 10^{12} m^{-2} for all as-received materials.

The hardness of as-received HEAs and 316H are shown in Table 3. The $Al_{0.3}CoCrFeNi$ was the hardest, followed by CoCrFeMnNi and then 316H. It should be stressed that the indentation size of nanoindentation (sub-micron) in this study was significantly smaller than 1/6 of the grain size of all materials (e.g. 100 μm/6 = 17 μm for 316H). According to Hou et al. [24], when the indent size is smaller than 1/6 of the grain size, indentations are not affected by grain-boundaries and do not follow the Hall-Petch relationship. Therefore, the hardness values of the three materials shown in Table 3 were not affected by their different grain sizes.

In summary, the as-received $Al_{0.3}CoCrFeNi$, CoCrFeMnNi and 316H exhibited a coarse grain structure, sparse inclusions, low dislocation density, and no precipitations or ordering phases. Therefore, the following irradiations were performed on nearly perfect matrixes without crystal defects such as grain/phase boundaries or dislocations, leaving the composition as the only independent variable in this study.

3.2. Irradiation effects on microstructure

The TEM micrographs in Figs. 5–7 show the microstructural evolution of HEAs and 316H irradiated at 300 °C with 1 MeV krypton ions to 1 dpa. The irradiated microstructures consist of a high density of dislocation loops. No void was observed.

Based on literature [25,26], irradiation-induced dislocation loops in HEAs and 316 SS are interstitial loops. For 316 SS, the loops produced under irradiation temperature of 300 °C are faulted frank loops with Burgers vectors of $b = \frac{a_0}{3}111$ lying on {111} planes [27,28]. The HEAs in this study share similar crystal structure and constituent elements with 316H, and may have the same loop characteristics.

The density and size of dislocation loops were measured and plotted as a function of irradiation dose in Fig. 8. The result indicates that the evolution of dislocation loops under irradiation at 300 °C was similar in the HEAs and 316H. This observation is consistent with the finding by Kumar et al. [9] in an ex-situ low-
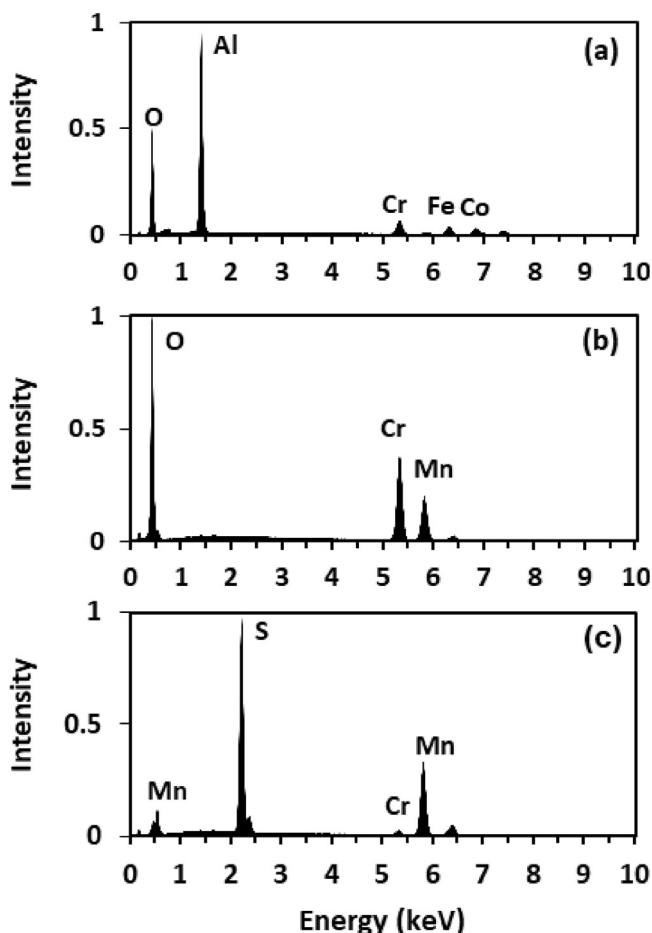
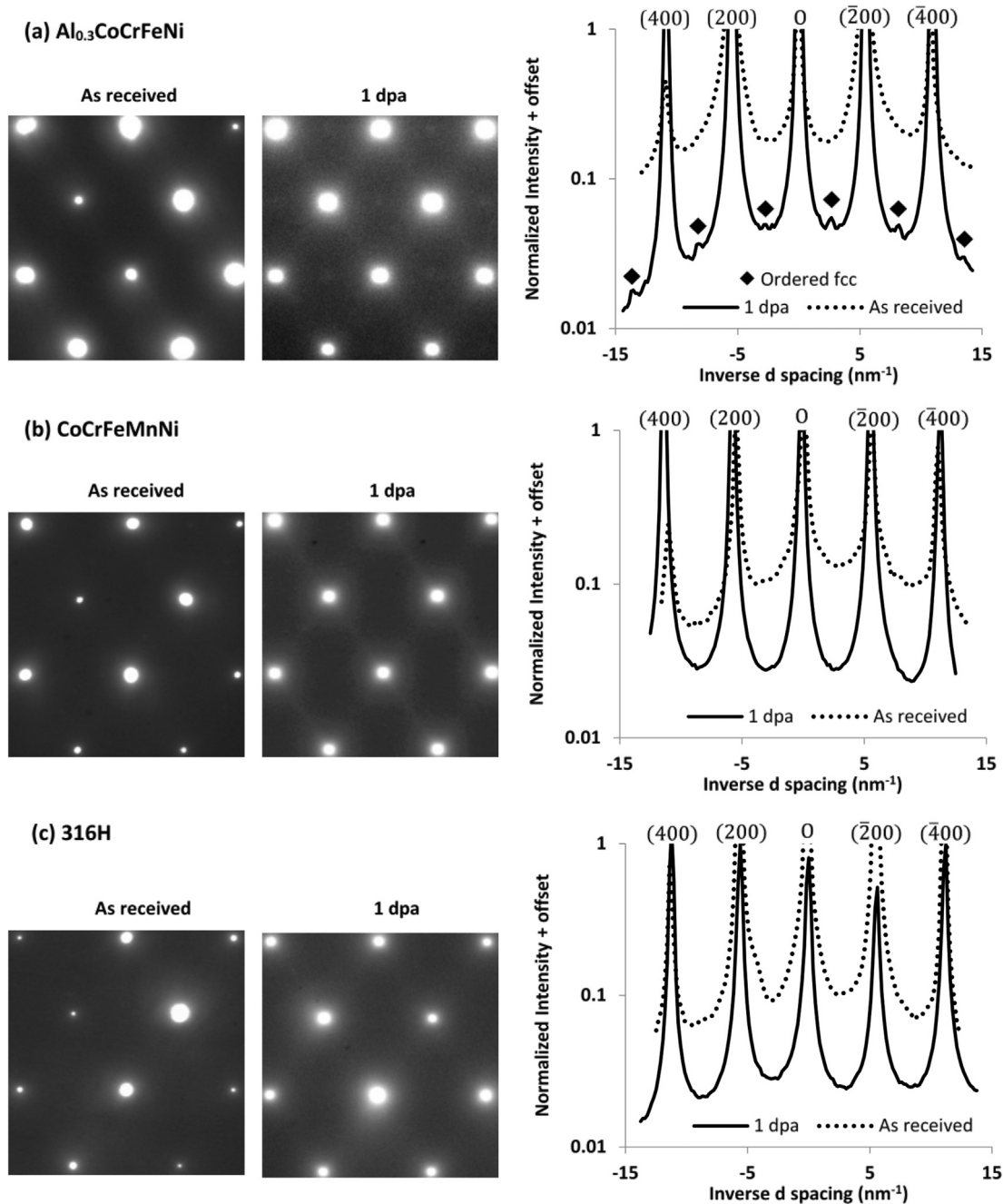**Fig. 4.** The 110 zone diffraction patterns and the corresponding intensity profiles along 200 g directions for (a) Al$_{0.3}$CoCrFeNi, (b) CoCrFeMnNi and (c) 316H before and after irradiation at 300 °C to 1 dpa. The brightness and contrast of the images had been adjusted to enhance the visibility of dark regions.

temperature irradiation experiment on FeNiMnCr HEA. As shown in Fig. 8, the dislocation loops appeared in all materials as early as 0.01 dpa, and the density increased with increasing dose until about 0.1 dpa when the density gradually saturated. The average size increased slightly with increasing dose, and the majority of the loops remained to be a few nanometers up to 1 dpa.

The observed dislocation loops agree well with the "black spot" irradiation defects reported in literature for austenitic stainless steels irradiated below 300 °C [26,29]. It has been shown that the microstructural evolution in austenitic stainless steels irradiated at this temperature range is insensitive to the composition (e.g. 316 vs. 347) [29]. The similar irradiated microstructures observed in HEAs and 316H implies that the above statement can be generalized to a

wider alloying space beyond iron-based austenitic steels. The compositional insensitivity may be related to the fact that the loop

Table 3
Nanoindentation measurements before and after ion irradiation.

	Al$_{0.3}$CoCrFeNi	CoCrMnFeNi	316H
As-received H$_o$ (GPa)	3.56 ± 0.05	3.14 ± 0.09	2.97 ± 0.04
After irradiation H$_{irr}$ (GPa)	4.63 ± 0.03	4.37 ± 0.12	3.98 ± 0.06
ΔH = H$_{irr}$-H$_o$ (GPa)	1.07 ± 0.06	1.23 ± 0.15	1.01 ± 0.07
ΔH$_c$ (GPa)	1.37	1.27	1.14

[†] The uncertainty of the measured hardness equals one standard deviation of the hardness data.

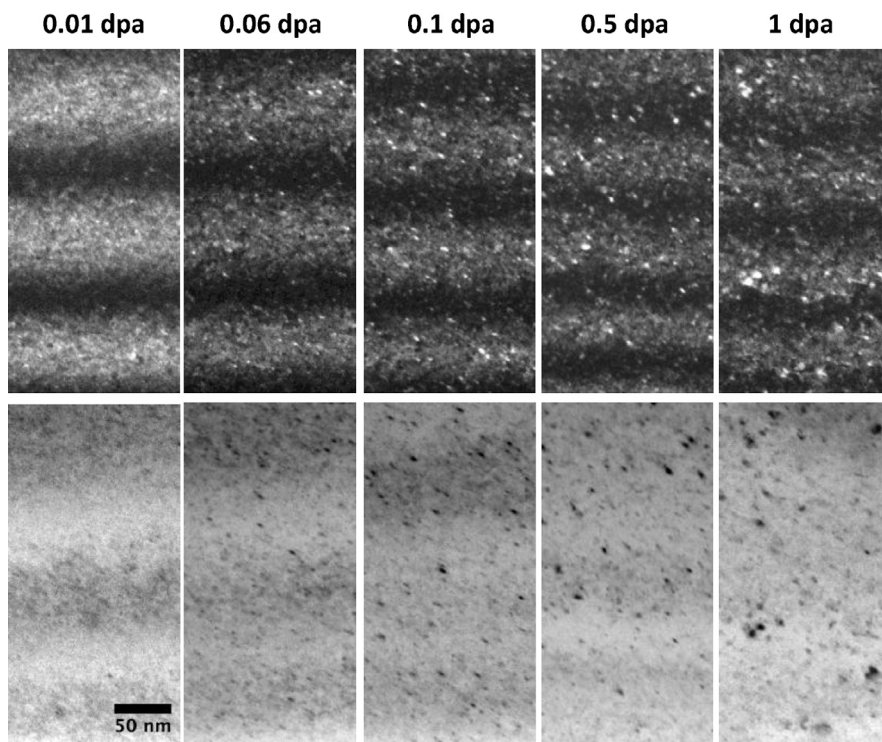**0.01 dpa** **0.06 dpa** **0.1 dpa** **0.5 dpa** **1 dpa**

Fig. 5. The WBDF (top) and BF (bottom) TEM micrographs of 316H irradiated with 1 MeV Kr ions at 300 °C. The WBDF diffraction condition was g = 200 (g, 6 g) at 011zone.

formation in fcc alloys at this temperature is largely by cascade condensation where long range diffusion of point defects is limited. As a result, the sluggish diffusion of HEAs has insignificant role in defect evolution, resulting in a similar size and density of irradiation-induced dislocation loops at this temperature.

As shown in Figs. 5–7, some line segments appeared in all samples at 1 dpa, mimicking the shape of large edge-on dislocation loops. However, detailed analysis with tilting indicates that the line contrast was in fact strings of small dislocation loops lining up to reduce strain energy. This observation may be understood with the
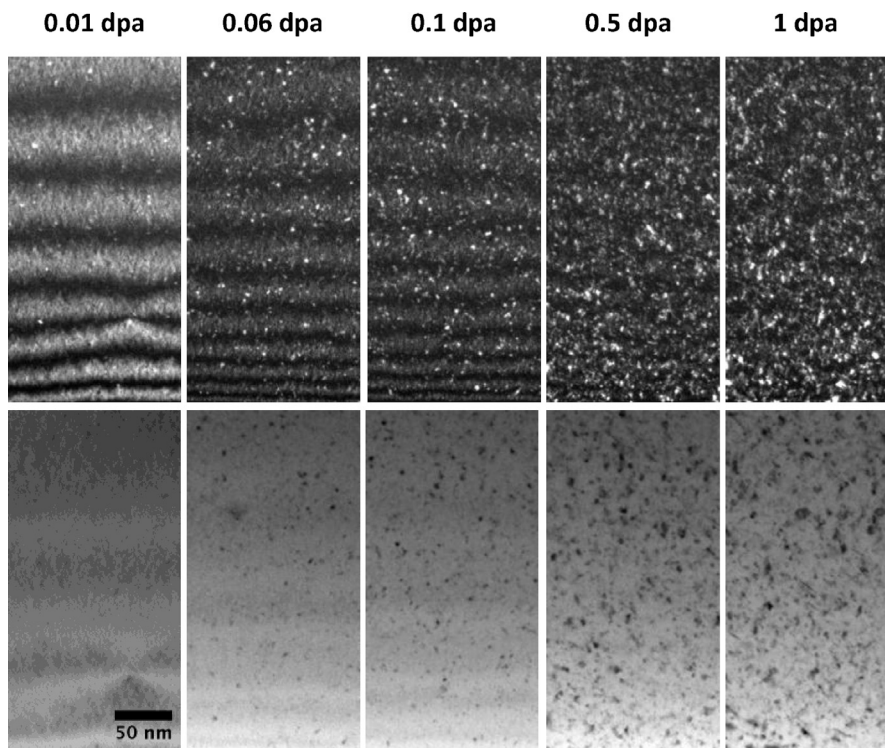
0.01 dpa **0.06 dpa** **0.1 dpa** **0.5 dpa** **1 dpa**

Fig. 6. The WBDF (top) and BF (bottom) TEM micrographs of CoCrFeMnNi irradiated with 1 MeV Kr ions at 300 °C. The WBDF diffraction condition was g = 200 (g, 6 g) at 011zone.
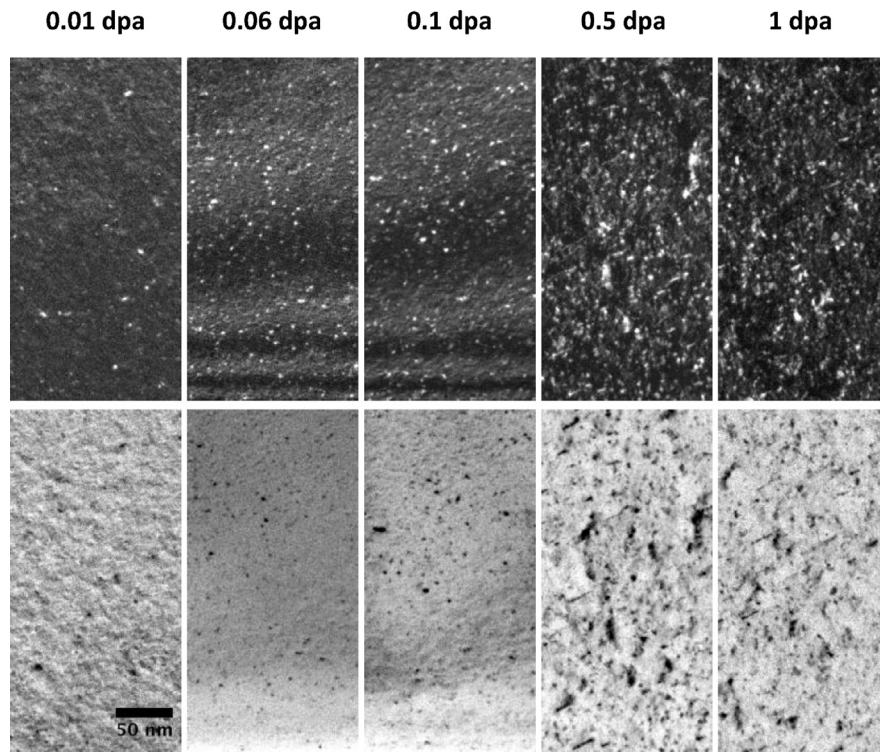
Fig. 7. The WBDF (top) and BF (bottom) TEM micrographs of $Al_{0.3}CoCrFeNi$ irradiated with 1 MeV Kr ions at 300 °C. The WBDF diffraction condition was g = 200 (g, 6 g) at 011 zone.

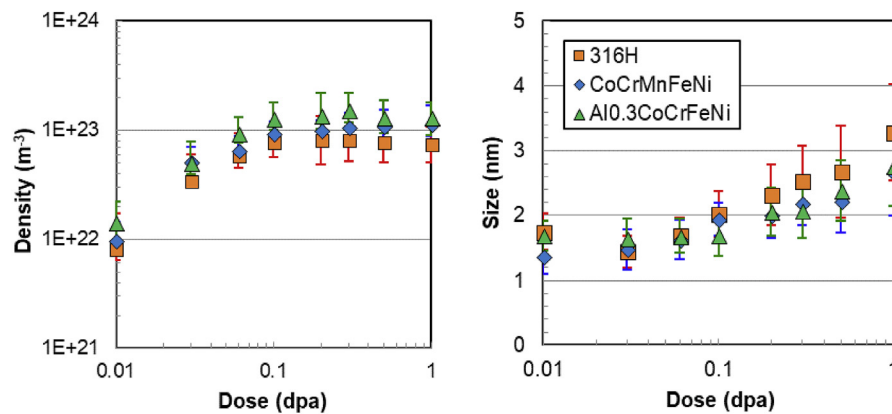**Fig. 8.** The density and size of irradiation-induced dislocation loops in 316H, CoCrFeMnNi and $Al_{0.3}CoCrFeNi$ irradiated with 1 MeV Kr at 300 °C. The error bar for the density measurement is described in section 2. The error bar of the size measurement corresponds to one standard deviation of the size distribution.

phenomenon reported in Ref. [30] where irradiation-induced defects interact and line up due to the influence of internal stress field. This string structure was more obvious in the thicker regions of the foils as shown in Fig. 9. Both HEAs and 316H exhibited a similar microstructure consisting of a high density of small dislocation loops and aligned structures. This kind of dislocation morphology was consistent with previous studies on the austenite phase in cast austenitic stainless steel irradiated with the same irradiation condition [31] and on tungsten alloys [32].

The phase stability of the HEAs and 316H was investigated with the electron diffraction patterns at 110 zone axis and the corresponding intensity profiles plotted along reciprocal lattice vectors ⟨200⟩ as shown in Fig. 4. For both 316H and CoCrFeMnNi, their matrix fcc structures remained stable, and no additional reflections were found after irradiation. In contrast, a trace of {100} reflections prohibited for a fcc structure at 110 zone axis were observed in

$Al_{0.3}CoCrFeNi$ after irradiation, which indicates the occurrence of ordering of the originally disordered fcc lattice. This observation shows that the single-phase microstructure of $Al_{0.3}CoCrFeNi$ is less stable than that of CoCrFeMnNi and 316H under irradiation at 300 °C. Also, considering the short irradiation time period (~4 h) and low temperature (300 °C), the observation of ordering signal in this study demonstrated an enhancement effect of irradiation on phase transformation.

The relatively low stability of $Al_{0.3}CoCrFeNi$ as compared with CoCrFeMnNi and 316H can be understood by its enthalpy and entropy of mixing, and relatively larger mismatch of atomic size. As proposed by Yang and Zhang [33], in a complex alloy system, a single-phase solid solution is favorable when its atomic mismatch δ is small ($\leq 6.6\%$), and the ratio of mixing entropy and enthalpy Ω is large (≥ 1.1):

Al₀.₃CoCrFeNi **CoCrFeMnNi** **316H**

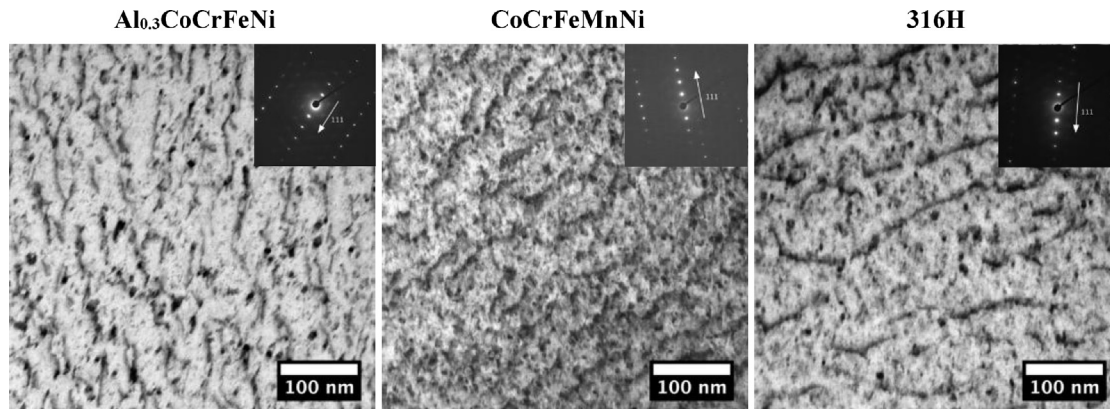**Fig. 9.** Bright-field TEM images of Al$_{0.3}$CoCrFeNi, CoCrFeMnNi and 316H irradiated with 1 MeV Kr at 300 °C to 1 dpa. Micrographs taken from the relatively thicker regions of the foil close to ($\bar{1}$10) zone axis where g = 111 was strongly reflected.

$$\delta = \sqrt{\sum_{i=1}^{n} c_i \left(1 - \frac{r_i}{\bar{r}}\right)^2}$$

$$\Omega = \frac{T_m \Delta S_{mix}}{|\Delta H_{mix}|}$$

$$\Delta S_{mix} = -R \sum_{i=1}^{n} c_i \ln c_i$$

$$\Delta H_{mix} = \sum_{i=1, \, i \neq j}^{n} 4 \Delta H_{ij}^{mix} c_i c_j$$

where c_i and r_i are the atomic percentage and the atomic radius of the ith component, respectively. $\bar{r} = \sum c_i r_i$ is the average atomic radius. T_m is the melting temperature. ΔS_{mix} and ΔH_{mix} are the mixing entropy and enthalpy, respectively. R is the gas constant. The ΔH_{ij}^{mix} is the enthalpy of mixing of binary liquid alloys. The atomic radius and the binary mixing enthalpy were obtained from Ref. [34] and Ref. [35], respectively. The values δ, ΔH_{mix}, ΔS_{mix}, T_m and Ω of Al$_{0.3}$CoCrFeNi, CoCrFeMnNi and 316H are given in Table 4.

Al$_{0.3}$CoCrFeNi has a larger δ than CoCrFeMnNi and 316H, which leads to a larger lattice distortion and strain energy. The Al$_{0.3}$CoCrFeNi has the smallest Ω among all three alloys, which indicates its higher tendency to decompose. Both of the parameters suggest that Al$_{0.3}$CoCrFeNi should exhibit poorer phase stability as compared with CoCrFeMnNi and 316H. In addition, as the Gibb free energy $G = H-TS$ (where H is enthalpy, T is absolute temperature and S is entropy), the effect of entropy on stabilizing solid solution phase was suppressed due to the relatively low irradiation temperature.

Since ordered L1$_2$ structure has often been observed as homogeneous spherical nanoparticles in aged and, in some studies, as-cast Al$_{0.3}$CoCrFeNi [23,36], centered dark field imaging using the

prohibited {100} diffraction spots was performed to search for the ordered precipitates in the irradiated Al$_{0.3}$CoCrFeNi. Nonetheless, no precipitates can be evidently revealed under TEM at 1 dpa.

It is possible that short-range ordering has taken place in the Al$_{0.3}$CoCrFeNi under irradiation without the nucleation and growth of long-range ordered (LRO) microdomains. As shown by Banerjee et al. in Ni$_4$Mo irradiated with 1 MeV electrons [37], the ordering process is sensitive to irradiation temperature. At temperature $-73\,°C \leq T_{irr} \leq 177\,°C$, the steady-state structure was short-range order (SRO). And at $177\,°C \leq T_{irr} \leq 447\,°C$, the steady state was a mixture of SRO and LRO. Above 447 °C, the steady-state structure was complete LRO. This temperature-dependent behavior is attributed to the mobility of point defects. At low temperatures, interstitials, but not vacancies, are mobile and only SRO can be maintained. The increasing stability of LRO with increasing T_{irr} was attributed to the increasing mobility of vacancies. The formation of SRO and the transition from SRO to LRO at low to intermediate temperatures was found to occur through a continuous mode consistent with concentration wave description. At high temperature $T_{irr} \geq 527\,°C$, ordering transformation proceeded with nucleation and growth mechanism.

The ordering mechanism in current study seems to fall in the low-to-intermediate temperature range described in Banerjee et al. where irradiation relocated atoms from the originally random fcc lattice in short range, resulting in a concentration wave of more ordered configuration, and at the same time compromising the destructive interference of {100} reflections in electron diffraction.

3.3. Irradiation hardening

The changes in the mechanical property of irradiated HEAs and 316H were studied using nanoindentation with a fixed indentation depth of 100 nm. Fig. 10 shows the representative load-displacement curves of CoCrFeMnNi before and after irradiation of 1 MeV krypton ions at 300 °C to 1 dpa. As shown in Table 3, the hardness of all materials increased by about 1 GPa after irradiation where the hardening was marginally higher for the HEAs than 316H.

Several factors can affect our nanohardness measurements, including the near-surface data scattering, indentation size effect and ion irradiation profile. As mentioned by Kumar et al. [9], the hardness data near a surface can vary due to surface irregularity. In our work, the specimens were prepared with electro-polishing, which produced a smooth and deformation-free surface with minimal surface irregularity. Therefore, a relatively smaller displacement of 100 nm can be used. This is supported by the fact of

Table 4
The parameters δ, ΔH_{mix}, ΔS_{mix} and Ω for HEAs and 316H.

	δ (%)	ΔH_{mix} (kJ mol^{-1})	ΔS_{mix} (JK^{-1}mol^{-1})	T_m (K)	Ω
Al$_{0.3}$CoCrFeNi	3.49	−7.27	12.83	1655	2.92
CoCrFeMnNi	0.92	−4.16	13.38	1562	5.02
316H[a]	1.47	−3.62	8.72	1673	4.03

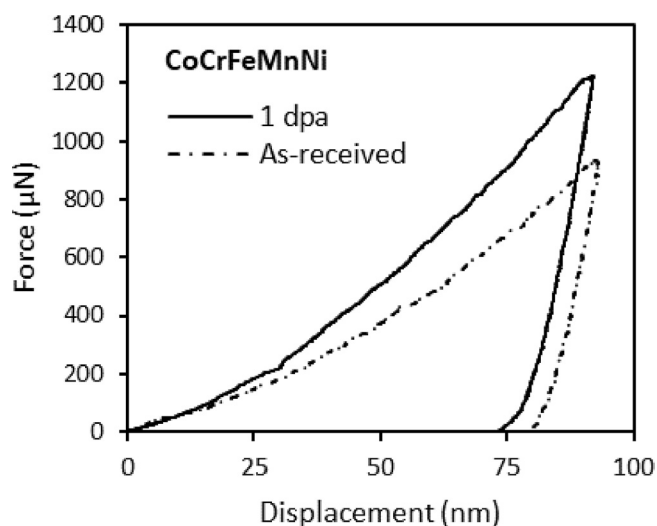[a] Calculation for 316H only considered Fe, Cr, Mn, Ni, Mo and Si.

Fig. 10. The representative nanoindentation load-displacement curves of CoCrFeMnNi before and after 1 MeV Kr^{2+} irradiation at 300 °C to 1 dpa.

very small data scattering being observed for all specimens.

The indentation size effect can also introduce some uncertainties. The hardness value increases with decreasing indentation size because a large strain gradient associated with a small indentation requires geometrically necessary dislocations for continuity [38]. To mitigate the size effect, indentations were performed to the same depth for all materials and irradiation conditions [39].

For irradiated samples, the hardness also depends on the dose profile. As shown in the SRIM calculation in Fig. 1 and MeV krypton ions produce an inhomogeneous damage profile that ends at about 500 nm for the Al$_{0.3}$CoCrFeNi, CoCrFeMnNi and 316H. Since the plastic zone of typical Berkovich tip is about five times the indentation depth [39], the 100 nm displacement used in this study roughly samples the entire dose profile with little contribution from the soft unirradiated substrate.

To correlate the irradiation hardening with microstructure, the Orowan hardening model and hardness-yield stress relationship by Higgy and Hammed [40] were used. The formulas are given as follows:

$$\Delta\sigma_y = M\alpha\mu b\sqrt{Nd}$$

$$\Delta H_c = K\Delta\sigma_y$$

where $\Delta\sigma_y$ and ΔH_c are the calculated increase in yield strength and hardness after irradiation, respectively. The Taylor factor M is 3.06 for equiaxed fcc. The barrier strength factor α of dislocation loops is 0.4 [41]. The shear modulus μ is 77 GPa, the same as that of austenitic steels. The Burgers vector b is $\frac{a_o}{2}110 = 0.257$ nm. The N and d are the density and size of the dislocation loops at 1 dpa, respectively. The constant K is 3 for irradiated austenitic stainless steels [42].

As shown in Table 3, the calculated increases in hardness ΔH_c for the three materials were similar, while it was slightly higher for the CoCrFeMnNi. Overall, the measured and calculated hardening values agree reasonably well. The discrepancy may be due to the uncertainties in nanoindentation measurement (size effect and ion dose profile), loop measurement (size and density) and the parameters of the hardening model (e.g. α and K).

In summary, the consistency between the calculated and measured hardening indicates that dislocation loops are the primary hardening source in both irradiated HEAs and 316H. The microstructural evolution and irradiation hardening are similar for Al$_{0.3}$CoCrFeNi, CoCrFeMnNi and 316H irradiated at 300 °C up to 1 dpa.

4. Conclusion

Two high entropy alloys, Al$_{0.3}$CoCrFeNi and CoCrMnFeNi, and a 316H SS were irradiated at 300 °C with 1 MeV krypton ions to 1 dpa with *in-situ* TEM observations. The irradiation damage resulted in a high density of dislocation loops in all three materials. A quantitative analysis showed that the size and density evolutions of dislocation loops were similar for the HEAs and 316H. Correspondingly, the nanoindentation hardness of both HEAs and 316H increased by about 1 GPa after irradiation. Short-range order was observed in the Al$_{0.3}$CoCrFeNi after irradiation, but not in CoCrFeMnNi and 316H. Overall, the behaviors of HEAs and 316H under irradiation at 300 °C were similar, possibly because most dislocation loops were formed through cascade condensation where the involvement of long-range diffusion of point defects was limited. Consequently, the features of HEAs that are supposed to be beneficial for irradiation resistance, such as sluggish diffusion and high configurational entropy, played little role in the microstructural evolution of HEAs at low irradiation temperatures. Future work on the irradiation effects of HEAs should focus on high irradiation temperatures where long-range diffusion of point defects is more pronounced.

References

[1] Y. Zhang, T.T. Zuo, Z. Tang, M.C. Gao, K.A. Dahmen, P.K. Liaw, Z.P. Lu, Prog. Mater. Sci. 61 (2014) 1–93.
[2] M.C. Gao, J.-W. Yeh, P.K. Liaw, Y. Zhang, High-entropy Alloys, Springer, 2016.
[3] K.-Y. Tsai, M.-H. Tsai, J.-W. Yeh, Acta Mater. 61 (13) (2013) 4887–4897.
[4] J.-W. Yeh, JOM (J. Occup. Med.) 65 (12) (2013) 1759–1771.
[5] M.-H. Tsai, J.-W. Yeh, Mater. Res. Lett. 2 (3) (2014) 107–123.
[6] C. Lu, L. Niu, N. Chen, K. Jin, T. Yang, P. Xiu, Y. Zhang, F. Gao, H. Bei, S. Shi, Nat. Commun. 7 (2016) 13564.
[7] C. Lu, T. Yang, K. Jin, N. Gao, P. Xiu, Y. Zhang, F. Gao, H. Bei, W.J. Weber, K. Sun, Acta Mater. 127 (2017) 98–107.
[8] M.-R. He, S. Wang, S. Shi, K. Jin, H. Bei, K. Yasuda, S. Matsumura, K. Higashida, I.M. Robertson, Acta Mater. 126 (2017) 182–193.
[9] N.K. Kumar, C. Li, K. Leonard, H. Bei, S. Zinkle, Acta Mater. 113 (2016) 230–244.
[10] K. Jin, C. Lu, L. Wang, J. Qu, W. Weber, Y. Zhang, H. Bei, Scripta Mater. 119 (2016) 65–70.
[11] S.J. Zinkle, L.L. Snead, Annu. Rev. Mater. Res. 44 (2014) 241–267.
[12] Y. Zhang, G.M. Stocks, K. Jin, C. Lu, H. Bei, B.C. Sales, L. Wang, L.K. Béland, R.E. Stoller, G.D. Samolyuk, Nat. Commun. 6 (2015) 8736.
[13] S. Shi, M.-R. He, K. Jin, H. Bei, I.M. Robertson, J. Nucl. Mater. 501 (2018) 132–142.
[14] W.-R. Wang, W.-L. Wang, J.-W. Yeh, J. Alloy. Comp. 589 (2014) 143–152.
[15] F. Otto, Y. Yang, H. Bei, E.P. George, Acta Mater. 61 (7) (2013) 2628–2638.
[16] D. Miracle, O. Senkov, Acta Mater. 122 (2017) 448–511.

[17] K. Natesan, M. Li, S. Majumdar, R. Nanstad, T.-L. Sham, Code Qualification of Structural Materials for AFCI Advanced Recycling Reactors, Argonne National Laboratory, 2012.

[18] J.W. Yeh, S.K. Chen, S.J. Lin, J.Y. Gan, T.S. Chin, T.T. Shun, C.H. Tsau, S.Y. Chang, Adv. Eng. Mater. 6 (5) (2004) 299—303.

[19] C.-J. Tong, Y.-L. Chen, J.-W. Yeh, S.-J. Lin, S.-K. Chen, T.-T. Shun, C.-H. Tsau, S.-Y. Chang, Metall. Mater. Trans. 36 (4) (2005) 881—893.

[20] W.-R. Wang, W.-L. Wang, S.-C. Wang, Y.-C. Tsai, C.-H. Lai, J.-W. Yeh, Intermetallics 26 (2012) 44—51.

[21] Ziegler, J. F.; Biersack, J.; Littmark, U., 1, Pergamon Press, New York 1985.

[22] X. Yi, M.L. Jenkins, K. Hattar, P.D. Edmondson, S.G. Roberts, Acta Mater. 92 (2015) 163—177.

[23] T.-T. Shun, Y.-C. Du, J. Alloy. Comp. 479 (1—2) (2009) 157—160.

[24] X. Hou, A. Bushby, N. Jennett, J. Phys. Appl. Phys. 41 (7) (2008), 074006.

[25] M.-R. He, S. Wang, K. Jin, H. Bei, K. Yasuda, S. Matsumura, K. Higashida, I.M. Robertson, Scripta Mater. 125 (2016) 5—9.

[26] S. Zinkle, P. Maziasz, R. Stoller, J. Nucl. Mater. 206 (2—3) (1993) 266—286.

[27] H. Brager, J. Straalsund, J. Nucl. Mater. 46 (2) (1973) 134—158.

[28] H. Brager, E. Gilbert, J. Straalsund, Radiat. Eff. Defect Solid 21 (1) (1974) 37—50.

[29] P. Maziasz, J. Nucl. Mater. 205 (1993) 118—145.

[30] M. Hernández-Mayoral, Z. Yao, M. Jenkins, M. Kirk, Phil. Mag. 88 (21) (2008) 2881—2897.

[31] W.-Y. Chen, M. Li, M.A. Kirk, P.M. Baldo, T. Lian, J. Nucl. Mater. 471 (2016) 184—192.

[32] X. Yi, M.L. Jenkins, M.A. Kirk, Z. Zhou, S.G. Roberts, Acta Mater. 112 (2016) 105—120.

[33] X. Yang, Y. Zhang, Mater. Chem. Phys. 132 (2—3) (2012) 233—238.

[34] C. Kittel, P. McEuen, P. McEuen, Introduction to Solid State Physics, vol. 8, Wiley, New York, 1996.

[35] A. Takeuchi, A. Inoue, Mater. Trans. 46 (12) (2005) 2817—2829.

[36] Q. Tang, Y. Huang, Y. Huang, X. Liao, T. Langdon, P. Dai, Mater. Lett. 151 (2015) 126—129.

[37] S. Banerjee, K. Urban, M. Wilkens, Acta Metall. 32 (3) (1984) 299—311.

[38] N. Fleck, G. Muller, M. Ashby, J. Hutchinson, Acta Metall. Mater. 42 (2) (1994) 475—487.

[39] P. Hosemann, D. Kiener, Y. Wang, S.A. Maloy, J. Nucl. Mater. 425 (1—3) (2012) 136—139.

[40] H. Higgy, F. Hammad, J. Nucl. Mater. 55 (2) (1975) 177—186.

[41] T. Byun, N. Hashimoto, K. Farrell, E. Lee, J. Nucl. Mater. 349 (3) (2006) 251—264.

[42] J.T. Busby, M.C. Hash, G.S. Was, J. Nucl. Mater. 336 (2—3) (2005) 267—278.